

Metasurface external cavity laser

Luyao Xu,^{1,2,a)} Christopher A. Curwen,^{1,2} Philip W. C. Hon,¹ Qi-Sheng Chen,³ Tatsuo Itoh,¹ and Benjamin S. Williams^{1,2}

¹Department of Electrical Engineering, University of California, Los Angeles, California 90095, USA

²California NanoSystems Institute, University of California, Los Angeles, California 90095, USA

³Northrop Grumman Aerospace Systems, Redondo Beach, California 90278, USA

(Received 5 September 2015; accepted 18 November 2015; published online 2 December 2015)

A vertical-external-cavity surface-emitting-laser is demonstrated in the terahertz range, which is based upon an amplifying metasurface reflector composed of a sub-wavelength array of antenna-coupled quantum-cascade sub-cavities. Lasing is possible when the metasurface reflector is placed into a low-loss external cavity such that the external cavity—not the sub-cavities—determines the beam properties. A near-Gaussian beam of $4.3^\circ \times 5.1^\circ$ divergence is observed and an output power level >5 mW is achieved. The polarized response of the metasurface allows the use of a wire-grid polarizer as an output coupler that is continuously tunable. © 2015 AIP Publishing LLC.

[<http://dx.doi.org/10.1063/1.4936887>]

Achieving a high quality beam—i.e., symmetric, directive, diffraction-limited, and non-astigmatic—is a challenge for many types of semiconductor lasers. This is particularly true as the waveguide size is increased to scale up the power, since multiple transverse mode oscillations can lead to sub-optimal beam quality as well as modal instabilities. One very successful solution that has been demonstrated in the visible and near-infrared is the vertical-external-cavity surface-emitting-laser (VECSEL), which can be thought of as a semiconductor version of a diode-pumped solid-state disk laser.¹ In a typical VECSEL configuration, a quantum well (or dot) semiconductor active medium is grown monolithically with a distributed Bragg reflector. When optically pumped over a large area, the semiconductor forms an active reflector as part of an external laser cavity. The cavity can be readily engineered to support only the fundamental Gaussian mode with near diffraction-limited beam quality—even at high output powers.^{2,3}

Beam quality has posed an even more difficult challenge for terahertz (THz) quantum-cascade (QC) lasers than for diode lasers. Terahertz QC-lasers almost exclusively use sub-wavelength metallic and/or plasmonic waveguides, which leads to highly divergent beams with large side-lobes unless special surface-emitting or antenna coupled geometries are used. Examples include 2nd order distributed feedback (DFB)^{4–6} and photonic crystal cavities⁷ which have achieved beam divergences as narrow as $\sim 9^\circ \times 6^\circ$. Further decreasing the beam divergence along both axes requires increasing the radiating aperture. However, if this is done by increasing the width of the waveguide, thermal performance suffers and multiple transverse modes can appear. Arrays of 2nd order DFBs is another option; however, on-chip phase locking is challenging for large numbers of array elements, and grating side-lobes appear if the array spacing is larger than the wavelength.^{6,8} End-fire 3rd order DFB QC-lasers are another attractive option with beams as narrow as $6^\circ \times 11^\circ$ and high slope efficiencies.^{9,10} However, further beam narrowing is

challenging because the divergence scales as the square root of the device length. The VECSEL approach is promising for addressing this challenge, but it has been impossible to implement for QC-lasers since the optical gain is based upon intersubband transitions of electrons within planar quantum wells.¹¹ These transitions obey an “intersubband selection rule” that only allows the interaction with the electric field polarized perpendicular to the wells, while in a VECSEL the polarization of the incident beam is naturally parallel to the quantum wells. While external cavity THz QC-lasers have been previously demonstrated, they were designed mainly for frequency tuning where the external cavities play no role in beam shaping or output coupling.^{12–14}

In this work, we report a THz VECSEL formed by an active metasurface reflector and a flat output coupler reflector, a schematic of which is given in Figure 1(a). Gain is provided by the active metasurface reflector, which couples surface incident radiation to the quantum-cascade gain medium, as shown in Figures 1(b) and 1(c). The metasurface is composed of a sparse array of metal-metal waveguide sub-cavities, which are spaced with a period Λ less than the free-space wavelength λ_0 , as shown in Figure 1(b). Each sub-cavity is a metal-metal ridge waveguide with width w , where the $10\text{ }\mu\text{m}$ thick GaAs/AlGaAs QC-laser active material is sandwiched between metal cladding above and below—similar to microstrip transmission line.¹⁵ Metal-metal waveguide is highly advantageous for THz QC-lasers; its optical modes are tightly confined to the active material, and its small geometry is beneficial for heat removal and continuous-wave (cw) operation.^{16–18} Here we use the waveguide in its first higher-order lateral mode (TM_{01}) at its resonant cutoff wavelength approximately determined by $w \approx \lambda_0/2n$, where n is the index of the semiconductor material. In this scenario, each sub-cavity essentially acts as an elongated patch antenna and strongly radiates in the surface direction.^{19–21} Due to its strong radiative loss each sub-cavity is intentionally a low-quality factor (Q) resonator and will not self-oscillate in this surface emitting mode (unlike other surface emitting structures such as resonant metasurface amplifiers²² or arrays of

^{a)}Electronic mail: luyaoxu.ee@ucla.edu

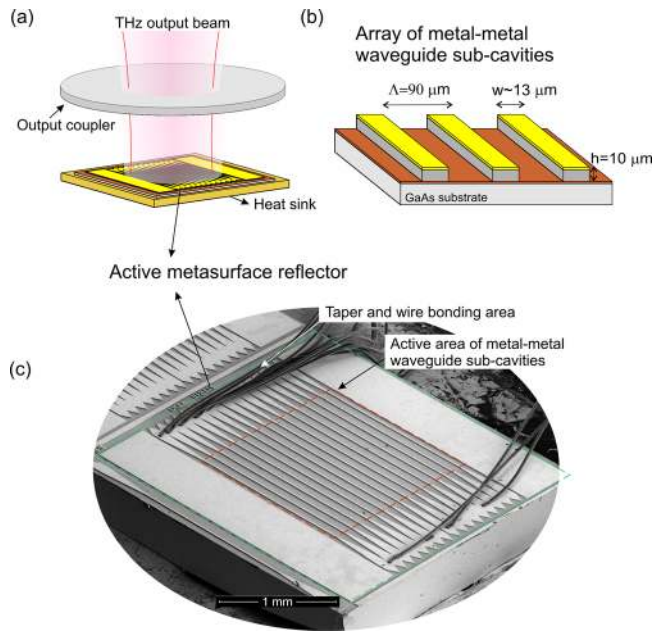


FIG. 1. (a) Schematic for a THz QC-VECSEL composed of an active metasurface reflector and an output coupler. (b) Detailed schematic of metal-metal waveguide sub-cavity array on the metasurface. (c) SEM image of an active metasurface reflector with a $1.5 \times 1.5 \text{ mm}^2$ active area.

2nd order DFBs⁶). When the sub-cavity array is placed within a high- Q external cavity, the array collectively provides gain to amplify the external cavity master mode such that lasing can occur. The structure of the master mode ensures phase coherence between stimulated emission from the radiating sub-cavities, and is the primary determinant of the beam and spectral properties of the laser. Another consideration is how to prevent each metal-metal waveguide from lasing in its own propagating TM_{00} mode (which could compete for gain with the desired TM_{01} mode). For this reason, each metal-metal sub-cavity ridge is terminated with an impedance transforming linear taper that connects to the region for wire bonding ($500 \mu\text{m}$ long, 5° flare angle); this area is kept electrically unbiased by depositing a dielectric layer underneath the top metallization. As the unbiased area will be lossy, this acts as an absorption boundary condition to reduce the waveguide facet reflection. Furthermore, the metallization of the tapered region along with the unbiased reflectors on each side of the active area ensures that the tails of the cavity mode see a highly reflecting surface.

A full-wave finite-element electromagnetic solver (Comsol Multiphysics 4.4) was used to simulate the reflectance spectra for a typical metasurface (period $\Lambda = 90 \mu\text{m}$ and ridge width $w = 13 \mu\text{m}$) including the effects of losses in the metal and semiconductor. As shown in Figure 2, the metasurface reflectance increases with the QC material gain coefficient g that is increased to simulate the effect of current injection and assumed uniform over the spectrum range considered. As the QC material gain coefficient g is increased above 20 cm^{-1} , net amplification is observed. Figure 2 also shows the curves of reflectance increasing with bulk gain g at three different frequencies, which confirms that bulk gain g is more efficiently coupled out to amplify the incident radiation when the operation frequency is closer to the resonant

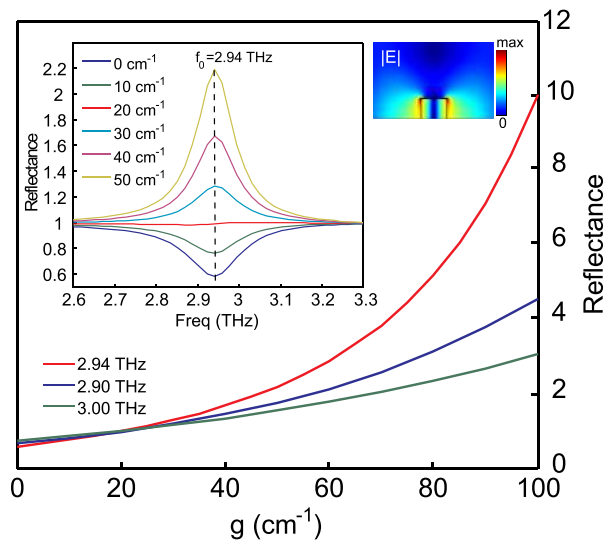


FIG. 2. The simulated reflectance change with the bulk gain g at three different frequencies for an active metasurface with metal-metal waveguide ridge width of $13 \mu\text{m}$ and height of $10 \mu\text{m}$, spaced in a period of $90 \mu\text{m}$. The left inset shows the simulated reflectance spectra for normally incident plane waves for different values of g . The right inset shows the electric field magnitude at resonance at 2.94 THz , where the electric field is predominantly polarized normal to the metal plane within the dielectric.

frequency (2.94 THz). Under normal incidence of radiation around the resonant frequency, the excited TM_{01} mode has its electric field inside the gain medium predominantly polarized perpendicular to the quantum wells, which satisfies the inter-subband polarization selection rule. Due to the low fill-factor of the metasurface with gain medium ($w/\Lambda \sim 15\%$), for a given injection current, a much larger emitting aperture is obtained than would be obtained by using a single large waveguide. The periodicity of $\Lambda = 90 \mu\text{m}$ is chosen to be slightly less than the free-space wavelength λ_0 to prevent Bragg scattering induced diffraction loss for normally incident waves, which is the major component of the external cavity mode. If needed, the periodicity could be further reduced to prevent Bragg scattering for obliquely incident waves (at the cost of greater power dissipation density). While the metasurface resonance frequency is primarily determined by the width of the ridge, there is a weak dependence on period as Λ approaches λ_0 due to mutual antenna coupling.

The fabrication of the active metasurface followed the standard steps for making metal-metal waveguides. Cu-Cu thermocompression bonding was used to bond the $10 \mu\text{m}$ thick active layer to a receiving wafer, followed by lapping and selective wet-etching of the substrate.²³ Then 200 nm of SiO_2 was deposited and patterned to isolate the taper and wire bonding area, followed by evaporation and lift-off of Cr/Au/Ni to provide the top metallization and self-aligned etch mask. The metal-metal waveguide ridges were then defined by the Chlorine-based dry etching with the subsequent removal of the Ni layer. The QC-laser gain medium used in this work is a resonant-phonon depopulation designed for peak gain at $\sim 2.9 \text{ THz}$, very similar to that described in Ref. 23. When measured in a conventional metal-metal waveguide device, it exhibits lasing from 2.7 to 3.7 THz under various bias conditions. Various metasurfaces were fabricated with

ridge widths varying from $11.5\ \mu\text{m}$ to $13.5\ \mu\text{m}$ to overlap with the QC material bulk gain peak. While several metasurfaces were observed to lase, we focus here on the best performing design with width $w = 12.5\ \mu\text{m}$; presumably this design has the best overlap of the gain spectrum with the metasurface resonance. Figure 1(c) shows a fabricated metasurface with an active area of $1.5 \times 1.5\ \text{mm}$ (i.e., 17 ridges). The metal-metal waveguides are electrically biased through the top metallization.

We demonstrated the THz QC-VECSEL in a plano-plano Fabry-Pérot (FP) cavity, as illustrated in Figure 4(a). The active metasurface device is mounted on a Cu submount within a cryostat, and a free-standing wire-grid THz polarizer (made of $20\text{-}\mu\text{m}$ diameter Tungsten wires spaced with a period of $50\ \mu\text{m}$) is mounted outside as an output coupler/mirror. The cryostat window is $\sim 3\ \text{mm}$ thick high-resistivity silicon (HR-Si) window, which also acts as an intracavity etalon with a free spectral range of $\sim 13\ \text{GHz}$. The total cavity length is about $6\ \text{mm}$. Although a plano-plano cavity is unstable and sensitive to misalignment, it still supports a fundamental mode with a near-Gaussian profile and relatively low loss. By using the iterative Fox and Li method²⁴ to model the intracavity circulating mode, we estimate $\sim 7\%$ round-trip diffraction loss due to finite metasurface size and $\sim 7\%$ from the absorption and reflection loss induced by the silicon etalon (i.e., cryostat window).²⁵ Due to the polarized response of both the metasurface and

output-coupler polarizer, one can increase the output coupling transmittance by varying the angle θ_p of the polarizer from 0° to 90° . θ_p is the angle between the polarizer's wire orientation and the direction transverse to the ridges on the metasurface. The precise dependence is non-trivial, as the output transmittance depends on the polarization state of the circulating laser field, which in turn depends on the co- and cross-polarized reflection coefficients of both the polarizer and metasurface.²⁵ As for any laser, there is an optimum coupling condition which maximizes the output power, which depends upon the interplay between the coupling loss and total loss, and its effect on threshold, the circulating power, and transmitted power. Figure 3(a) shows power vs. current (P - I) and voltage vs. current (V - I) measurement curves for a set of orientation angles from 0° to 24° at $77\ \text{K}$. The P - I - V characteristics were measured in pulsed mode (0.25% overall duty cycle, 500 ns-long pulses repeated at $10\ \text{kHz}$, modulated by a slow $5\ \text{Hz}$ pulse train with lock-in detection). A calibrated pyroelectric photodetector was mounted close to the output coupler polarizer without any intermediate optics for power measurement. At $77\ \text{K}$, the output power is maximized at a value of $1.15\ \text{mW}$, which is achieved with $\theta_p = 18^\circ$. The threshold current density and slope efficiency both increase with θ_p as shown in Figure 3(b), which is consistent with an increasing out-coupling loss. For $\theta_p > 24^\circ$, out-coupling loss becomes too high for the VECSEL to reach the lasing threshold. Figure 3(c) shows the differential conductance (dI/dV) for each angle. The discontinuity at threshold is observed to be lower as θ_p is increased, which is consistent with a longer upper state lifetime due to reduced stimulated emission and reduced circulating intensity under higher out-coupling loss conditions. When the polarizer is removed to destroy the external cavity, no lasing power is measured and the discontinuity disappears. Only in one outlier device at $6\ \text{K}$ was

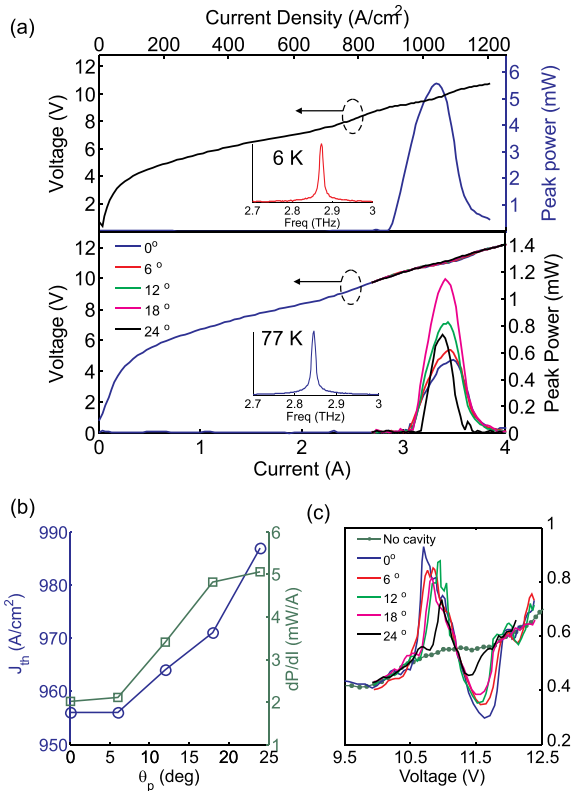


FIG. 3. (a) Upper: pulsed mode P - I - V characteristic and spectrum at $6\ \text{K}$, with polarizer angle $\theta_p = 30^\circ$. Lower: pulsed mode P - I - V characteristics for angle θ_p varied from 0° to 24° at $77\ \text{K}$. The inset is the lasing spectrum. (b) Measured threshold current density J_{th} and slope efficiency dP/dI versus with θ_p at $77\ \text{K}$. (c) Differential conductance curves in the lasing range for different θ_p and no cavity case at $77\ \text{K}$.

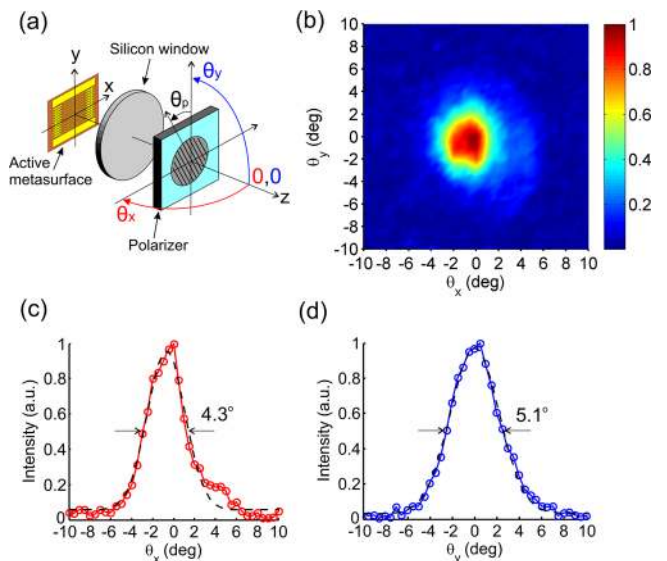


FIG. 4. Beam pattern. (a) The schematic for the VECSEL cavity setup and beam pattern measurement scheme. (b) Measured beam pattern measured for the THz QC-VECSEL at $77\ \text{K}$. (c) and (d) One-dimensional cut of the beam pattern through the intensity maximum along θ_x and θ_y angular directions, with Gaussian curve fit (dashed black line).

lasing observed to occur without the polarizer; this occurred at very high threshold and at a frequency (~ 3.6 THz) far away from the metasurface resonance of 2.8–2.9 THz.

Due to the larger gain present at 6 K, the optimum coupling condition is reached at a larger polarizer angle of $\theta_p = 30^\circ$. The maximum output power is measured to be 5.5 mW, with a slope efficiency of 16.7 mW/A (equivalent to ~ 0.008 photons/electron/stage), as shown in Figure 3(a). This value is somewhat lower than expected; a detailed analysis of possible sources of inefficiency is given in Ref. 25. We believe significant improvement can be expected by reducing sources of cavity loss (i.e., excess metasurface absorption, diffraction loss, cryostat window absorption), designing the cavity mode to overlap the metasurface more uniformly, and better alignment of the QC material gain spectrum with the metasurface resonance. The present VECSEL dissipates more than 30 W, which is not suitable for cw operation at cryogenic temperatures. However, because the narrow active region ridges (~ 13 μm) is favorable for heat removal, we believe that the VECSEL configuration is advantageous for cw operation provided the total power consumption is reduced to a moderate level, perhaps by using a different active region design with lower threshold current density or by reducing the total active area of the metasurface.

The measured far-field beam pattern is quite symmetric and directive as shown in Figure 4(b), which is directly measured after the polarizer as shown in Figure 4(a). The one-dimensional cuts of the beam pattern through the center along θ_x and θ_y directions are given in Figures 4(c) and 4(d), which show good fits with Gaussian curves. The full-wave half-maximum (FWHM) divergence angle is about 4.3° in the θ_x direction and 5.1° in the θ_y direction. The low-divergence near-Gaussian beam pattern aligns with the fact that the plano-plano FP cavity can support a quasi-stable cavity mode with a near-Gaussian mode profile, and is close to the calculated beam divergence based on Fox-and-Li method.²⁵

At 77 K the emission spectrum is single-mode at 2.846 THz (within the ~ 7 GHz resolution limit of our spectrometer), and is unchanged with adjustments in electrical bias, cavity length, or polarizer angle. Tuning the cavity length by moving the polarizer in the axial direction only results in turn-on and -off of lasing, caused by the longitudinal mode phase matching. It is believed that this single mode behavior results from the etalon effect of the HR-Si window in combination with the limited resonant frequency range of the metasurface. The spectrum is also measured at 6 K in pulsed mode and shows single-mode lasing at 2.873 THz. The shift of 27 GHz of the lasing frequency from 6 K to 77 K represents two longitudinal mode hops in the FP cavity, i.e., approximately twice the ~ 13 GHz free spectral range of the HR-Si window etalon. This mode hopping is presumably a result of the metasurface's reflection peak and phase change and the active medium's gain profile change with temperature.

In summary, the demonstration of a metasurface VECSEL initiates a promising approach towards achieving THz lasers with high-quality beam patterns and significant levels of power. This prototype exhibited a near-Gaussian

output beam pattern with low divergence ($4.3^\circ \times 5.1^\circ$). Furthermore, the polarized response of the metasurface allows one to use a wire-grid as a continuously adjustable output coupler to optimize output power and efficiency for a given operating condition. Considerable room exists for further improvement of THz QC-VECSELs to achieve higher output power and efficiency, cw operation, and an even narrower far-field beam patterns. The intra-cavity access of the VECSEL has the potential to provide tremendous versatility to QC-lasers, such as spectral tuning and filtering, spatial mode shaping, and polarization control. Furthermore, while we use a homogeneous active metasurface here, the VECSEL approach gives the ability to leverage ongoing advances in inhomogeneous metasurfaces and reflectarrays to design phase, spectral, polarization, and spatial properties of the intra-cavity field and emitted beams.^{26–28}

This work was partially supported by NSF ECCS Grant Nos. 1150071 and 1407711. Microfabrication was performed at the UCLA Nanoelectronics Research Facility, and wire bonding was performed at the UCLA Center for High Frequency Electronics.

¹A. C. Tropper, H. D. Foreman, A. Garnache, K. G. Wilcox, and S. H. Hoogland, *J. Phys. D: Appl. Phys.* **37**, R75 (2004).

²M. Kuznetsov, F. Hakimi, R. Sprague, and A. Mooradian, *IEEE Photonics Technol. Lett.* **9**, 1063 (1997).

³B. Rudin, A. Rutz, M. Hoffmann, D. J. H. C. Maas, A.-R. Bellancourt, E. Gini, T. Südmeyer, and U. Keller, *Opt. Lett.* **33**, 2719 (2008).

⁴S. Kumar, B. S. Williams, Q. Qin, A. W. M. Lee, Q. Hu, and J. L. Reno, *Opt. Express* **15**, 113 (2007).

⁵G. Xu, R. Colombelli, S. P. Khanna, A. Belarouci, X. Letartre, L. Li, E. H. Linfield, A. G. Davies, H. E. Beere, and D. A. Ritchie, *Nat. Commun.* **3**, 952 (2012).

⁶Y. Halioua, G. Xu, S. Moumdji, L. Li, J. Zhu, E. H. Linfield, A. G. Davies, H. E. Beere, D. A. Ritchie, and R. Colombelli, *Opt. Express* **23**, 6915 (2015).

⁷Y. Chassagneux, R. Colombelli, W. Maineult, S. Barbieri, H. E. Beere, D. A. Ritchie, S. P. Khanna, E. H. Linfield, and A. G. Davies, *Nature* **457**(7226), 174 (2009).

⁸T.-Y. Kao, Q. Hu, and J. L. Reno, *Appl. Phys. Lett.* **96**, 101106 (2010).

⁹M. I. Amanti, M. Fischer, G. Scalari, M. Beck, and J. Faist, *Nat. Photonics* **3**, 586 (2009).

¹⁰T.-Y. Kao, Q. Hu, and J. L. Reno, *Opt. Lett.* **37**, 2070 (2012).

¹¹R. Köhler, A. Tredicucci, F. Beltram, H. E. Beere, E. H. Linfield, A. G. Davies, D. A. Ritchie, R. C. Iotti, and F. Rossi, *Nature* **417**, 156 (2002).

¹²L. Mahler, A. Tredicucci, F. Beltram, H. E. Beere, and D. A. Ritchie, *Opt. Express* **18**, 19185 (2010).

¹³A. W. M. Lee, B. S. Williams, S. Kumar, Q. Hu, and J. L. Reno, *Opt. Lett.* **35**, 910 (2010).

¹⁴J. Xu, J. M. Hensley, D. B. Fenner, R. P. Green, L. Mahler, A. Tredicucci, M. G. Allen, F. Beltram, H. E. Beere, and D. A. Ritchie, *Appl. Phys. Lett.* **91**, 121104 (2007).

¹⁵C. A. Balanis, *Antenna Theory-Analysis and Design* (Wiley-Interscience, Hoboken, NJ, 2005).

¹⁶B. S. Williams, S. Kumar, H. Callebaut, Q. Hu, and J. L. Reno, *Appl. Phys. Lett.* **83**, 2124 (2003).

¹⁷B. S. Williams, *Nat. Photonics* **1**, 517 (2007).

¹⁸M. Wienold, B. Röben, L. Schrottke, R. Sharma, A. Tahraoui, K. Biermann, and H. T. Grahn, *Opt. Express* **22**, 3334 (2014).

¹⁹A. A. Tavallae, B. S. Williams, P. W. C. Hon, T. Itoh, and Q.-S. Chen, *Appl. Phys. Lett.* **99**, 141115 (2011).

²⁰P. W. C. Hon, A. A. Tavallae, Q.-S. Chen, B. S. Williams, and T. Itoh, *IEEE Trans. Terahertz Sci. Technol.* **2**(3), 323 (2012).

²¹Y. Todorov, L. Tosetto, J. Teissier, A. M. Andrews, P. Klang, R. Colombelli, I. Sagnes, G. Strasser, and C. Sirtori, *Opt. Express* **18**, 13886 (2010).

²²T.-Y. Kao, J. Reno, and Q. Hu, *Intersubband Transitions in Quantum Wells* (Bolton Landing, NY, 2013).

- ²³B. S. Williams, S. Kumar, Q. Hu, and J. L. Reno, *Opt. Express* **13**, 3331 (2005).
- ²⁴A. G. Fox and T. Li, *Bell Syst. Tech. J.* **40**, 453 (1961).
- ²⁵See supplementary material at <http://dx.doi.org/10.1063/1.4936887> for cavity mode and beam pattern modeling, and slope efficiency calculation.
- ²⁶N. Yu and F. Capasso, *Nat. Mater.* **13**, 139 (2014).
- ²⁷A. V. Kildishev, A. Boltasseva, and V. M. Shalaev, *Science* **339**, 1232009 (2013).
- ²⁸D. M. Pozar, S. D. Targonski, and H. D. Syrigos, *IEEE Trans. Antennas Propag.* **45**, 287 (1997).